Chapter-2

SHEATH PLASMA RESONANCE IN INVERTED FIREBALLS

***Abstract**: The sheath plasma resonance (SPR) in an inverted fireball (IFB) system is semi-analytically investigated in the framework of a generalized hydrodynamic (electron-ion bifluidic) isothermal model formalism. It incorporates the constitutive ionic fluid viscosity, inter-species collisions, and geometric curvature effects. The SPR stability is studied for an anodic (hollow, meshed) IFB for the first time against the traditional cathode-plasma arrangements of regular electrode (solid, smooth) fireballs. The SPR develops in the vicinity of a spherical electrode enclosed by a plasma sheath amid a given electric potential. A generalized linear quartic dispersion relation (DR) with diverse plasma multi-parametric dispersion coefficients is methodically derived using a standard spherical normal mode analysis. The mathematical construct of the DR roots confirms that there exists only one feasible nonzero frequency mode (emerging in the IFB). This DR root is studied both analytically and numerically*[†]*. This consequent SPR creates trapped acoustic fluctuations in the IFB plasmas because of the internal reflections at the sheath plasma boundary. Also, sensible parametric changes in the SPR features, with both plasma density and viscosity, are seen. A local condition for the SPR excitation and its subsequent transition to collective standing wave-like patterns in the IFBs is illustratively analyzed. A fair corroboration of our investigated results with the earlier SPR experimental observations of standing wave-like eigenmode patterns (evanescent) validates the practical reliability of this theoretical study.*

2.1 INTRODUCTION

Any electrode with adequately raised electrostatic potential (relative to the ionization and plasma potentials) in a surrounding plasma can create a plasma fireball (FB) on its surface or within it, if a solid or hollow meshed anode is used, respectively [1, 2]. These two distinct types of laboratory FBs based on their different anode morphology are characterized as regular fireball (RFB) and inverted fireball (IFB), respectively. Due to the greater electrostatic potential, the drifting electrons acquire velocities fast enough to excite or even ionize the neutrals through inelastic collisions. Thus, they form the plasma FB glow inside the sheath region around the anode [3].

[†] Dutta, S. and Karmakar, P. K. Analytic model for sheath plasma resonance in inverted fireball, *https://arxiv.org/abs/2411.05397*.

The spatial dimension of the laboratory plasma FBs is determined by the electron-ion flux balance (floating condition) through the plasma boundary [1]. It is noteworthy to add here that a highly nonlinear double layer (DL) forms around a FB. This DL gathers charges from the ambient plasma and accelerates them subsequently. It also detaches the sheath region from the ambient plasma [3]. It is pertinent to note that any imbalance of the particle flux across DL may instigate various instabilities, which are, in fact, of great interest for both fundamental as well as applied research [4].

One of such instabilities is the sheath plasma resonance (SPR) instability discussed in this chapter. The sheath formed in an FB is spatiotemporally dynamic in nature. The circumventing sheath and the plasma inside an IFB undergo oscillations. It may so happen that the oscillating plasma sheath may start resonating with the trapped plasma inside the IFB under some circumstances. This may lead to an instability termed as the SPR instability [5, 6]. It has a number of applications in both fundamental and applied fields of great value. A few of such applications are enumerated at the end of this chapter summarily.

2.2 MODEL EQUATIONS

We consider a simpler, magnetic field free IFB system (of spherical geometry) as shown in Fig. 1.1(b). The considered spherical symmetry of the IFB reduces the analysis into a one-dimensional (radial) problem. The individual dynamics of the two fluids (electrons-ions) fulfil the plasma conditions $((r,t) \gg (\lambda_D, \omega_p^{-1}))$. The local imbalance of charges within the DL surrounding the IFB induces a non-neutral local charge number density ($n_e \neq n_i$). The constitutive number density fields in the electrical Poisson equation develop the corresponding potential dispersal as a useful closure property. The DR is finally obtained by decoupling the continuity and momentum equations amid the Poisson equation. The DR is solved both analytically (with a few reasonable approximations) and numerically (without any approximation). It turns out that in many cases the analytical approximation is sufficient to describe the IFB system very well. The unique analytical solution of the DR describes the angular frequency (and its harmonics) generated in the system. In the numerical solution, only one out of the four roots yield feasible plots without any singularity and discontinuity. This single root generates 2-D and 4-D profiles that are in good agreement with the ones analytically developed for similar plasma parameters. The two sets of equivalent results along with the various comparable 2-D and 4-D profiles finally describe the SPR behavior of the system.

The SPR dynamics is analyzed with local linear perturbation theory. The corresponding sets of governing equations are given as follows
The continuity equation for electrons (ions)

$$\partial_t n_{e(i)} + \vec{\nabla}.\left(n_{e(i)}\vec{v}_{e(i)}\right) = 0. \tag{2.1}$$

The total number of particles in a definite volume varies only upon changes in the particle flux across the surfaces enclosing the volume [7].

The momentum equation for electrons (ions) is given by

$$m_{e(i)}n_{e(i)}\left[\partial_t\vec{v}_{e(i)} + \left(\vec{v}_{e(i)}.\vec{\nabla}\right)\vec{v}_{e(i)}\right] = -\vec{\nabla}\mathrm{P} \mp en_{e(i)}\vec{E} + \eta\left(\nabla^2\vec{v}_{e(i)}\right) + \left(\zeta + \frac{\eta}{3}\right)\vec{\nabla}\left(\vec{\nabla}.\vec{v}_{e(i)}\right) + \vec{p}_{ei(ie)}. \tag{2.2}$$

The net force exerted on the charges is expressed in terms of the individual parametric forces exerted on them, i.e., due to the pressure gradient ($\vec{\nabla}P$), electric field ($\vec{E}$), spatial velocity variation ($\nabla^2\vec{v}_{e(i)}$), and momentum gain of electronic fluid due to collision with ions ($\vec{p}_{ei(ie)}$), and vice versa [7, 8]. Poisson equation yields the electrostatic potential distribution in terms of the charge density in the generic notations [9] reads as

$$\nabla^2\phi = 4\pi e(n_e - n_i). \tag{2.3}$$

Here, $n_{e(i)}, \vec{v}_{e(i)}, m_{e(i)}, P, e, \vec{E}, \zeta, \eta$, and $\vec{p}_{ei(ie)}$ denote the charge number density, velocity, mass of electrons (ions), thermal pressure, electronic charge, local electric field, bulk viscosity, shear viscosity in the medium, and momentum gain due to plasma constituent collisions in the medium, respectively.

It may be highlighted that an electron-depleted sheath and a field-free cold plasma in a plasma system behave as a capacitor and inductor, respectively. A small-scale perturbation can instigate unstable oscillations in the peripheral sheath and in the plasma region within the field free IFB. The SPR can yield plasma oscillations resonating with the sheath [5]. This resonance occurs when the electron transit time across the sheath is equivalent to the inverse of electron plasma frequency (ω_{pe}). Therefore, the electron transit time helps to anticipate the SPR frequency in an IFB system discussed herein [6].

In this work, we emphasize the SPR-induced oscillations in an IFB system under laboratory conditions. The SPR is also linked to the sheath plasma instability (SPI) discussed herein and in reference [5, 6]. This work uses a linear perturbation formalism of the governing equations of an IFB system that finally leads to a quartic equation for the angular instability frequency ω.

It is noteworthy that the SPR instabilities have so far been reported only in connection with classical RFB like arrangements [5, 6]. Studies in IFB systems haven't been conducted yet as far as noticed. Thus, the main motivation of this chapter is to study such resonance instability phenomena within the IFBs. Besides, a bifluidic ansatz is used in this work for the first time to describe the IFBs with variations in density, viscosity, and linear small-scale perturbation of the involved parameters. This theoretical model recreates a few of the experimental outcomes on the IFBs reported previously in the literature.

2.3 STABILITY ANALYSIS

The local stability analysis of the considered sheath plasma system is performed with the standard technique of linear normal mode analysis in spherically symmetric geometry. Accordingly, the relevant physical variables (F) are linearly perturbed (F_1) with respect to their corresponding hydrostatic homogenous equilibrium values (F_o), presented symbolically [10] as

$$F(r,t) = F_o + F_1(r,t) = F_o + F_{10}\left(\frac{1}{r}\right)\exp[-i(\omega t - kr)], \tag{2.4}$$

$$F = [n \;\; v \;\; \phi]^T, \tag{2.5}$$

$$F_o = [n_o \;\; 0 \;\; 0]^T, \tag{2.6}$$

$$F_1 = [n_1 \;\; v_1 \;\; \phi_1]^T. \tag{2.7}$$

Inside the IFB the charged particle velocity is usually constant, and the electric field is zero. However, there can be sudden changes due to electron or ion bunching or their transit through the IFB leading to a locally nonzero electric field, especially on the edges. The $1/r$-factor originates as an outcome of spherical symmetry in the perturbations of the relevant plasma fluid parameters ($v_{e(i)}$ and $n_{e(i)}$), as clearly shown in Eq. (2.4). The $1/r$-dependency drops out for any planar geometry and the perturbation acquires the usual plane-wave form, given as $F_{10}\exp[-i(\omega t - kr)]$ [11, 12]. It enables us to transform our physical model from the defined spherical coordination space $(r,\ t)$ to the Fourier wave space $(k,\ \omega)$ with the linear differential operator equivalence relationships, defined as $\partial_t(\equiv -i\omega)$, $\nabla\ \ (= \nabla_r \equiv (ik - 1/r))$, $\nabla^2(= \nabla_r^2 \equiv (r^{-2})\partial_r(r^2\partial_r) = \partial_r^2 + (2r^{-1})\partial_r \equiv (2r^{-2} - k^2 - 2ikr^{-1}) + (2ikr^{-1} - 2r^{-2}) = -k^2)$, and so forth [10]. The terms k and ω are wavenumber and angular frequency of the perturbation, respectively. Thus, the exponent quantity, $[-i(\omega t - kr)]$, represents the argument of the homologous considered fluctuations. It hereby yields the fluctuation phase velocity as $v_p = \omega/k$ and group velocity as $v_g = c_s^2/v_p = kc_s^2/\omega$, $c_s = \sqrt{k_B T_e/m_i}$, being the ion acoustic phase velocity.

We use a standard linear perturbation formalism, as constructed in Eqs. (2.4)-(2.7), over Eqs. (2.1)-(2.3) for the electron (ion) dynamics. The equilibrium number density, $n_{e(i)o} = n_c\exp(-\gamma r^2) = n_o$, is applied here in accordance with the previously reported experimental data [13]. The symbol, n_c, denotes the constant electron (ion) number density inside the IFB center. This internal density distribution usually follows a Gaussian (normal) shape with $\gamma = 1/2\sigma^2$; where, σ denotes the standard deviation (dispersion) from the central maximum in the symmetrical bell-shaped profile [13]. Accordingly, Eq. (2.1) is employed to describe the perturbed electronic (ionic) dynamics in usual notations [9] as

$$-i\omega n_{e(i)1} + n_{e(i)o}\left(ik + \frac{1}{r}\right)v_{e(i)1} - 2\gamma[rn_c\exp\left(-\gamma r^2\right)]v_{e(i)1} = 0. \tag{2.8}$$

We simplify Eq. (2.8) in terms of $n_{e(i)1}$ and $v_{e(i)1}$, as written below

$$n_{e(i)1} = \left(\frac{1}{i\omega}\right)\left(ik + \frac{1}{r} - 2\gamma r\right)n_o v_{e(i)1}. \tag{2.9}$$

We apply the same formalism in Eq. (2.2) for the electron (ion) dynamics in the plasma governed by the isothermal classical equation of state. The expressions for the thermal pressure, $P = n_o k_B T_e$, and for the linear momentum gain due to the interparticle (ambipolar) collisional dynamics, $p_{ei(ie)} = [\pi\left(en_{e(i)o}\right)^2 m_e^{1/2}/(4\pi\epsilon_o)^2(k_B T_e)^{3/2}]\,v_{e(i)1}$, are adopted from the literature [7]. Further, $p_{ei(ie)}$ is used as $p_o n_o^2 v_{e(i)}$ for the sake of brevity. Accordingly, Eq. (2.2) with these substitutions reads as

$$-i\omega m_{e(i)}n_{e(i)o}v_{e(i)1} = -\left(ik-\frac{1}{r}\right)k_BT_en_{e(i)1} \mp \left(ik-\frac{1}{r}\right)en_{e(i)o}\phi_1 - \left(\zeta+\frac{\eta}{3}\right)\left(k^2+\frac{2}{r^2}\right) - \eta k^2 v_{e(i)1} + p_o n_o^2 v_{e(i)1}. \tag{2.10}$$

We simplify Eq. (2.10) in terms of $v_{e(i)1}$, $n_{e(i)1}$, and ϕ_1 as follows

$$v_{e(i)1} = \frac{k_BT_e\left(ik-\frac{1}{r}\right)n_{e(i)1} \pm en_o\left(ik-\frac{1}{r}\right)\phi_1}{i\omega m_{e(i)}n_o - \left[\left(\zeta+\frac{4\eta}{3}\right)k^2+\left(\zeta+\frac{\eta}{3}\right)\frac{2}{r^2}\right]+p_on_o^2}. \tag{2.11}$$

Using the coefficients of viscosity terms, $\xi = (\zeta + 4\eta/3)$ and $\beta = (\zeta + \eta/3)$ as the effective generalized fluid viscosity and compound fluid viscosity, respectively, the Eq. (2.11) is modified as

$$v_{e(i)1} = \frac{k_BT_e\left(ik-\frac{1}{r}\right)n_{e(i)1} \pm en_o\left(ik-\frac{1}{r}\right)\phi_1}{i\omega m_{e(i)}n_o - \left(\xi k^2+\frac{2\beta}{r^2}\right)+p_on_o^2}. \tag{2.12}$$

Further, substituting Eq. (2.12) in Eq. (2.9) for $v_{e(i)1}$ and after rearrangements, we have

$$n_{e(i)1} = \frac{\pm en_o^2\left(ik-\frac{1}{r}\right)\left(ik-2\gamma r+\frac{1}{r}\right)\phi_1}{\left[i\omega\left\{i\omega m_{e(i)}n_o-\left(\xi k^2+\frac{2\beta}{r^2}\right)+p_on_o^2\right\}-n_ok_BT_e\left(ik-\frac{1}{r}\right)\left(ik-2\gamma r+\frac{1}{r}\right)\right]}. \tag{2.13}$$

We finally apply the same perturbation scheme (Eqs. (2.4)-(2.7)) for ϕ_1 in Eq. (2.3) with the application of the Laplacian operator in spherical coordinates and arrive at the following equation

$$-k^2\phi_1 = 4\pi e(n_{e1}-n_{i1}). \tag{2.14}$$

The substitution of n_{e1} and n_{i1} from Eq. (2.13) in Eq. (2.14) results in

$$-k^2\phi_1 = 4\pi e^2 n_o^2\left[\frac{1}{i\omega\left\{i\omega m_en_o-\left(\xi k^2+\frac{2\beta}{r^2}\right)+p_on_o^2\right\}-n_ok_BT_e\left(ik-\frac{1}{r}\right)\left(ik-2\gamma r+\frac{1}{r}\right)} - \frac{1}{i\omega\left\{i\omega m_in_o-\left(\xi k^2+\frac{2\beta}{r^2}\right)+p_on_o^2\right\}-n_ok_BT_e\left(ik-\frac{1}{r}\right)\left(ik-2\gamma r+\frac{1}{r}\right)}\right]\left(ik-\frac{1}{r}\right)\left(ik-2\gamma r+\frac{1}{r}\right). \tag{2.15}$$

We simplify Eq. (2.15) for the non-trivial condition $\phi_1 \neq 0$ to yield the following generalized quartic linear dispersion relation (DR)

$$A\omega^4 + B\omega^3 + C\omega^2 + D\omega + E = 0. \tag{2.16}$$

Clearly, Eq. (2.16) has a unique set of multi-parametric dispersion coefficients cast respectively as

$$A = 1, \tag{2.17}$$

$$B = i\left\{\left(\frac{1}{m_e n_o}\right)\left(\xi k^2 + \frac{2\beta}{r^2}\right) - \left(\frac{m_i p_o n_o}{m_e}\right)\right\}, \tag{2.18}$$

$$C = \left\{\left(\frac{k_B T_e}{m_e}\right)\left(ik - \frac{1}{r}\right)\left(ik - 2\gamma r + \frac{1}{r}\right) - \left(\frac{1}{m_e m_i n_o^2}\right)\left(\xi k^2 + \frac{2\beta}{r^2}\right)^2 + \left(\frac{2p_o}{m_e m_i}\right)\left(\xi k^2 + \frac{2\beta}{r^2}\right) - \left(\frac{p_o n_o^2}{m_e m_i}\right) - \left(\frac{4\pi e^2 n_o}{m_e}\right)\left(ik - \frac{1}{r}\right)\left(ik - 2\gamma r + \frac{1}{r}\right)\frac{1}{k^2}\right\}, \tag{2.19}$$

$$D = i\left\{\left(\frac{2k_B T_e}{m_e m_i n_o}\right)\left(\xi k^2 + \frac{2\beta}{r^2}\right)\left(ik - \frac{1}{r}\right)\left(ik - 2\gamma r + \frac{1}{r}\right) - \left(\frac{2p_o n_o k_B T_e}{m_e m_i}\right)\left(ik - \frac{1}{r}\right)\left(ik - 2\gamma r + \frac{1}{r}\right)\right\}, \tag{2.20}$$

$$E = \left(\frac{(k_B T_e)^2}{m_e m_i}\right)\left(ik - \frac{1}{r}\right)^2\left(ik - 2\gamma r + \frac{1}{r}\right)^2. \tag{2.21}$$

To feed the magnitudes of the involved parameters for numerical analysis of Eq. (2.16), we correlate it with an experimentally reported hydrogen plasma system [5]. This experimental work fairly offers the relevant IFB parametric magnitudes in this context. This is how it helps in anticipating the practical magnitudes of the diverse ω-coefficients for our DR analysis to proceed. Accordingly, the considered typical experimental values below, suitably taken from the literature [5], enables us to solve the DR analytically. The relevant parametric values are [5]: $m_e = 9.1 \times 10^{-31}$ kg, $m_i = 1.67 \times 10^{-27}$ kg, $e = 1.6 \times 10^{-19}$ C, $n_c = 10^{14} - 10^{17}\ \mathrm{m}^{-3}$, $n_o = n_c \exp(-\gamma r^2)$, $k_B T_e = 3.2 \times 10^{-19}$ J, $\xi \approx \beta = 10^{-5}\ \mathrm{N\ s\ m^{-2}}$, $\gamma = 510\ \mathrm{m}^{-2}$, and $p_o = 2.42 \times 10^{-42}\ \mathrm{kg\ m^3\ C^{-2}\ s^{-1}}$. Besides, since $m_i \gg m_e$ ($m_e/m_i = 5.45 \times 10^{-4}$), we take $m_i \pm m_e \approx m_i$.

Application of the above parametric inputs in Eqs. (2.18)-(2.21) presents

$$B = 1.18i \times 10^{10}\left(k^2 + \frac{2}{r^2}\right)\exp(\gamma r^2), \tag{2.22}$$

$$C = -3 \times 10^{16} \left(k^2 + \frac{2}{r^2}\right) \exp(2\gamma r^2), \tag{2.23}$$

$$D = 2.27i \times 10^{18} \left(k^2 + \frac{2}{r^2}\right) \left(ik - \frac{1}{r}\right) \left(ik - 2\gamma r + \frac{1}{r}\right) \exp(\gamma r^2), \tag{2.24}$$

$$E = 1.68 \times 10^{19} \left(ik - \frac{1}{r}\right)^2 \left(ik - 2\gamma r + \frac{1}{r}\right)^2. \tag{2.25}$$

The SPR frequency is expected to be of the order of the electron plasma frequency ($\sim 10^{11} - 10^{12}$ Hz) [5, 6]. Assuming an ω-value on this magnitude order, the first three terms $A\omega^4$, $B\omega^3$, and $C\omega^2$ from Eq. (2.16) are found to possess equivalent magnitudes ($\sim 10^{40} - 10^{44}$). The approximate magnitudes of the $D\omega^1$- and $E\omega^0$-terms in Eq. (2.16) are 10^{28} and 10^{19}, respectively. These are far smaller than the first three terms. Hence, we ignore these two lower-order terms and move forward with the first three higher-order terms in Eq. (2.16) justifiably. The reduced form of Eq. (2.16) is cast as

$$(A\omega^2 + B\omega^1 + C)\omega^2 = 0. \tag{2.26}$$

Using the dispersion coefficients A from Eq. (2.17), B from Eq. (2.22), and C from Eq. (2.23) in Eq. (2.26), we evaluate the dispersion roots as

$$\omega_1 = 0, \tag{2.27}$$

$$\omega_2 = 0, \tag{2.28}$$

$$\omega_3 = 0, \tag{2.29}$$

$$\omega_4 = -1.18i \times 10^{10} \left(k^2 + \frac{2}{r^2}\right) \exp(\gamma r^2). \tag{2.30}$$

It may be noticed that the expression in Eq. (2.30) is the first coefficient of ω^3 in the DR (Eq. (2.16)). The expression is independent of ion mass, which is a possible variable to different background plasmas. So, Eq. (2.30) can be used (extrapolated) to find out the general solution for SPR dynamics in any laboratory plasmas. Therefore, the general solution for the SPR in the IFB system is given as

$$\omega_4 = -i\left(\frac{1}{m_e n_c}\right)\left(\xi k^2 + \frac{2\beta}{r^2}\right)\exp(\gamma r^2). \tag{2.31}$$

The absence of any real component in $\omega = \omega_4$ in Eq. (2.31) indicates that this SPI branch is not propagatory. The negative imaginary feature of ω_4 points at the stable (with certain conditions) and standing wave-like nature of the SPR. It means that the instability gets reflected from the sheath region. So, the electron plasma frequency in the sheath (ω_{spe}) must be higher than the instability frequency (ω_4), else it will leak through the IFB anode. Consequently, the IFB does not act as a cavity resonator. In addition, the DR (Eq. (2.16)) is also solved numerically with the same set of parametric values. The detailed analytic calculations leading to the derived numerical solutions are skipped for spatiotemporal limitations. Here, the analytical and numerical DR roots are conjointly illustrated for a common multi-parametric comparison graphically. It is observed through comparison that both analytical and numerical figures are in good agreement with each other. It ensures the reliability of the analytical solution, Eq. (2.31), with some reasonable approximations.

5.4 RESULTS AND DISCUSSIONS

The dynamics of the excited SPR inside an IFB is studied with a linear perturbation formalism in laboratory spatiotemporal scales in spherical geometry. This linear formalism is applicable under the assumption of small amplitude perturbations [14]. The assumed spherical symmetry makes the polar and azimuthal coordinates within the IFB redundant in the SPR description. This symmetry simplifies the linear analysis by reducing the IFB dynamics into a one-dimensional (radial) problem.

The linear first-order perturbation analysis transforms the IFB model into a generalized linear quartic DR (Eq. (2.16)) with multiparametric coefficients (Eqs. (2.17)-(2.21)). To evaluate the contribution of each of the terms along with their coefficients, the values of all the involved constants, such as e, $m_{e(i)}$, p, n_o, and $k_B T_e$ are applied from experimentally reported hydrogen plasma IFB system [5].

It may be noted that the terms, such as r^2, k^2, and $n_o = n_c \exp(-\gamma r^2)$ do not vary with the background plasma but vary with the IFB plasma parameters. During the SPR, the two parameters k and r are mathematically linked through the 'resonance condition' $rk = (4\pi)^{-1}$. The viscosity coefficients, ξ and β are specific to the host plasma used for exciting the SPR phenomena. Therefore, it may be inferred, from Eq. (2.30), that the common mode of the SPR in any IFB plasma system is given as $\omega = -i(1/m_e n_c)(\xi k^2 +$

$2\beta/r^2)\exp(\gamma r^2)$. Applying the experimentally reported values of the various relevant parameters, the SPR mode can be evaluated for that specific IFB plasma system.

The colormap of the SPR dynamics (via Eq. (2.16)) reveals diverse multi-parametric properties. These analyses comprise of results obtained from the analytical solution (only ω_i) as well as the numerical solution (both ω_r and ω_i). It is important to add that $\omega_r > 0$ and $\omega_r < 0$ denote the propagating and evanescent nature of the perturbations [15], respectively. Whereas $\omega_i > 0$ and $\omega_i < 0$, on the other hand, denote the growth and decay of the perturbations [15]. In the case of $\omega_r = 0$, the SPR is a pure standing wave (non-propagatory), i.e., the nodes and antinodes of the wave formed within the IFB remain spatially invariant over time. For a direct comparison of the results from two different methods (analytical and numerical), the plots are arranged correspondingly. The various 2-D plots (Figs. 2.1-2.5, Figs. 2.9-2.12) demonstrate the $\omega_{i(r)}$-variation with respect to r or k for different $\xi(\approx \beta)$, n_c, and γ-values. Similarly, the 4-D colormaps (Figs. 2.6-2.8, Figs. 2.13-2.14) show the variation of $\omega_{i(r)}$ with respect to $n_o(r)$, $\chi\ (= \xi k^2 + 2\beta/r^2)$, r or k at the common resonance condition $[rk = (4\pi)^{-1}]$.

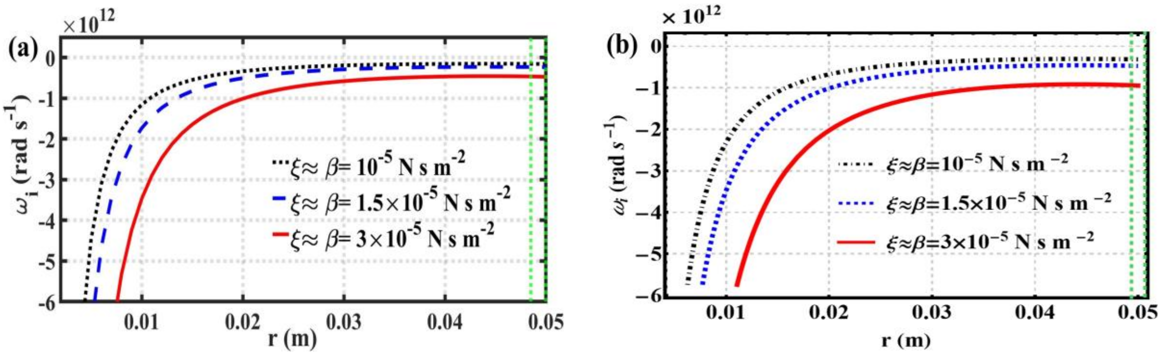

Figure 2.1: *Profile of the spatial variation of the imaginary frequency part (ω_i) of the DR obtained for different displayed ξ-values (a) analytically and (b) numerically.*

The distinct lines in Fig. 2.1 link to $\xi(\approx \beta) = 10^{-5}$ N s m^{-2} (black dotted line), 1.5×10^{-5} N s m^{-2} (blue dashed line), 3×10^{-5} N s m^{-2} (red solid line), respectively. The two external parallel green dotted lines denote the IFB sheath regions in both the subplots.

The highest SPI growth amplitude ($\propto \omega_i$) occurs close to the sheath region inside the IFB, where the plasma density, and hence, the plasma viscosity ($\chi \propto n_{e(i)}/v_{e(i)}$ [16]) are at their lowest magnitudes. The condition, $\omega_i \approx 0$, indicates the inability of the IFB system to damp the applied perturbation in that sheath vicinity region. The spatial variation of $\omega_i = f(r)$ (Figs. 2.1-2.2) across the IFB implies a variable response of the IFB plasma towards the SPI. The peripheral IFB sheath region is favorable to the SPI (with higher ω_i-value), whereas the central denser region shows a rapid decrease in the ω_i-value. It replicates an evanescent wave with gradually decaying amplitude, $F_{10}\exp(\omega_i t)$, towards the center of the IFB system. Since the plasma number density $[n_o = n_c \exp(-\gamma r^2)]$ has its maximum (n_c) at the IFB center ($r = 0$), it clearly proves that n_o damps the SPI.

There exists a minor difference in the radial ω_i-profiles (obtained from Eq. (2.16)) relative to the IFB center constructed analytically (Fig. 2.1(a)) and numerically (Fig. 2.1(b)). This disparity is clearly attributable to the approximate calculations carried out in the former and exact calculations in the latter. Consequently, the curves in analytical plots start growing a bit closer to the IFB center because the electron population density increases in that region. Since all the involved terms are considered in numerical analysis without any approximation, these terms make some small (nonzero) contributions to the effective plasma density. Thus, this instability grows a bit further radially away from the center in the numerical counterpart (Fig. 2.1(b)) against the analytical one (Fig. 2.1(a)). Besides, three different values of the viscosities (ξ and β) are considered herein for a broader representation of the instability results in a wider viscosity horizon of real importance.

The physics behind the SPR excitation may be explained with the inductor (L) and capacitor (C)-like behavior of the field free IFB plasma and the sheath, respectively. As the interior of the IFB is field free and consists mainly of cold electrons, it behaves inductively and can become resonant to its surrounding sheath, which essentially acts as a capacitor [5, 6]. As discussed in [5], this LC resonant circuit exhibits an unstable antiresonance, that depends only weakly on the IFB electrode bias. Instability occurs due to negative RF sheath resistance during the SPR, when the electrons also start to behave inertially along with the ions. The SPR occurs most efficiently in the ideal case, when $\omega/\omega_p \approx 1$. Furthermore, the instability is strongly damped at the plasma potential.

The electron density increases towards the center of the IFB and so does the plasma frequency. Hence, it approaches the limit $\omega/\omega_p \to 0$. In this extreme case, the resonant part of the wave is extinguished, while the antiresonance that drives the SPI is strongly damped, a result that also corroborates the experimental findings [5]. The results of our model, which indicate this behavior, are also graphically described as follows.

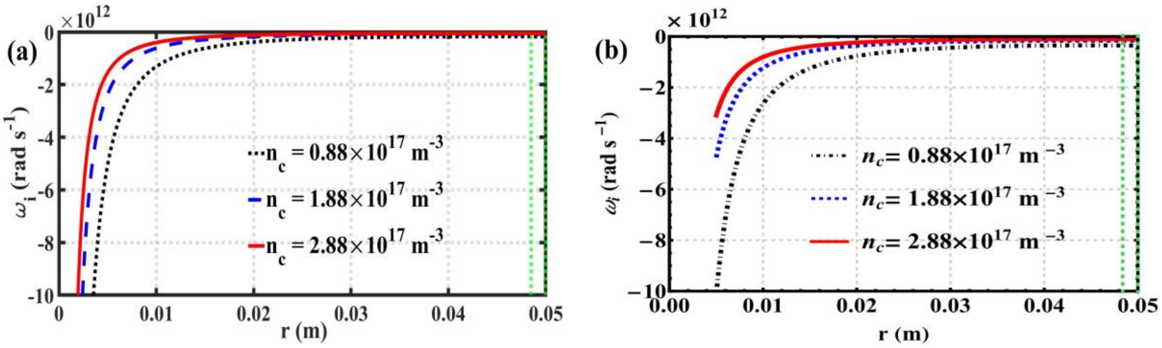

Figure 2.2: *Profile of the spatial variation of the imaginary frequency part (ω_i) of the DR obtained for different displayed n_c-values (a) analytically and (b) numerically.*

The distinct lines in Fig. 2.2 link to $\mathrm{n_c}= 0.88 \times 10^{17}\ \mathrm{m^{-3}}$ (black dotted line), $1.88 \times 10^{17}\ \mathrm{m^{-3}}$ (blue dashed line), $2.88 \times 10^{17}\ \mathrm{m^{-3}}$ (red solid line), respectively. The two external parallel green dotted lines denote the IFB sheath regions in both the subplots.

It may be concluded from Fig. 2.2 that the IFB center is most stable against any introduced SPR perturbation. The SPR, which originates in the sheath region, is also strongest there and dies out while approaching the center. The wavelength of the acoustic wave produced due to SPR is equivalent to the diameter of the IFB anode. This indicates that the IFB can act as a cavity resonator holding an SPR induced standing wave. It may also be pointed out that there is no qualitative variation in ω_i noticed against the central density (n_c) apart from the meagre change in ω_i-magnitude.

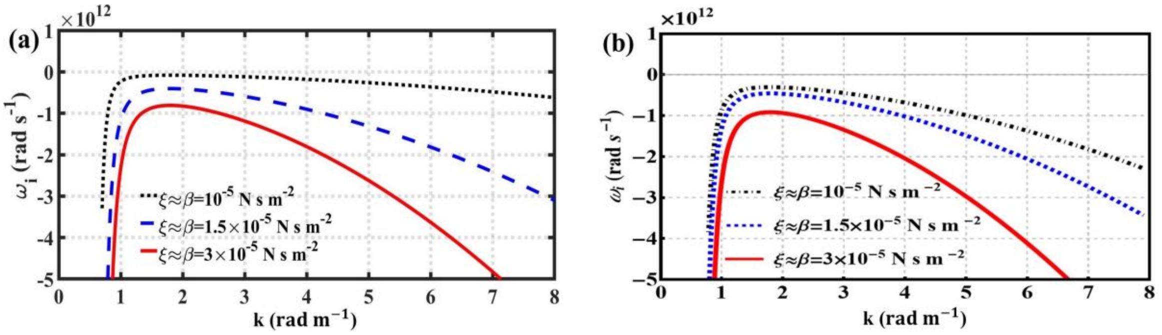

Figure 2.3: *Profile of the imaginary frequency part (ω_i) variation of the DR obtained for different ξ-values with respect to k (a) analytically and (b) numerically.*

Applying the IFB resonance condition of $rk = (4\pi)^{-1}$, the final solution of the DR (Eq. (2.30)) is expressed in terms of wave number k through both the analytical (Fig. 2.3(a)) and numerical (Fig. 2.3(b)) profiles. The modified form which reads $\omega_i = -316.51k^2(1/m_e n_c)\exp(\gamma/16\pi^2 k^2)$, is plotted for various values of $\xi(\approx \beta) = 10^{-5}\ \mathrm{N\,s\,m^{-2}}$ (black dotted line), 1.5×10^{-5} $\mathrm{N\,s\,m^{-2}}$ (blue dashed line), and 3×10^{-5} $\mathrm{N\,s\,m^{-2}}$ (red solid line)). The different $\xi(\approx \beta)$-values are used herein to study variations of the SPR properties for different viscosities. The SPI shows a sudden rise with respect to k with subsequent fall at higher k-values. The ω_i-variation in the k-space corresponds to Fig. 2.1 for r.

The ω_i-variation in the k-space represents a growth (or decay) rate of the SPI for different wavelengths or frequencies of the applied perturbation. It also means that effective plasma behavior differs for different wavelengths of perturbation. It is seen quite often that the growth (or decay) rate of the instability does not have a linear correlation with k. The k-value corresponding to the maxima of ω_i-variation may be depicted as the resonance point where the perturbation grows most rapidly.

Moreover, when looking at the instability frequency in the k-space (Fig. 2.3), one sees a distinctive maximum in ω_i in this domain. The reason for this becomes evident from a closer inspection of the DR solution, Eq. (2.31). Keeping in mind that the wavenumber k is proportional to r^{-1}, one can see that in the case of small k (or large r) the exponential term in Eq. (2.31) becomes dominant while the prefactor vanishes. However, the exponential term goes to 1 for $r \rightarrow 1$, which leads to a peak in the $\omega_i(k)$-function close to the IFB center.

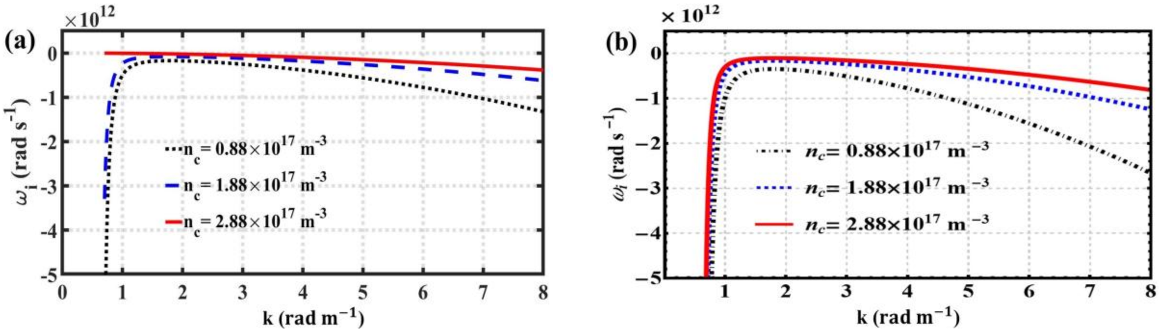

***Figure 2.4**: Profile of the imaginary frequency part (ω_i) variation of the DR obtained for different n_c-values with respect to k (a) analytically and (b) numerically.*

It is noteworthy that a good agreement between the analytical and numerical results proves the semi-analytic accuracy and reliability of the proposed SPR calculation scheme. It is quite apparent that n_c does not have any qualitative influence on ω_i, as also observed earlier. However, the exponential drop in the plasma density towards the edge of the IFB influences oscillations considerably. The corresponding ω_i curves for three different n_c-magnitudes at smaller k-values are indistinctly merged. The different n_c-magnitudes are used herein to examine variations of the SPR properties for different densities. The basic physics behind such ω_i-variations remains the same as already explained before in Fig. 2.3. The observed ω_i-maxima occurs at $k \approx 1.4\ \mathrm{rad\ m^{-1}}$ to $1.6\ \mathrm{rad\ m^{-1}}$, which corresponds to, from $r = 5.6 \times 10^{-2}$ m to 4.9×10^{-2} m, perfectly covering the sheath region ($r \approx 5 \times 10^{-2}$ m or 5 cm) with the resonance condition $[rk = (4\pi)^{-1}]$. The oscillation amplitude is maximum beside the sheath region due to the SPR, like an antinode in a standing wave. Therefore, the specific r corresponding to the k where the ω_i-maxima occurs, holds the antinode forming due to the SPR excited inside the IFB.

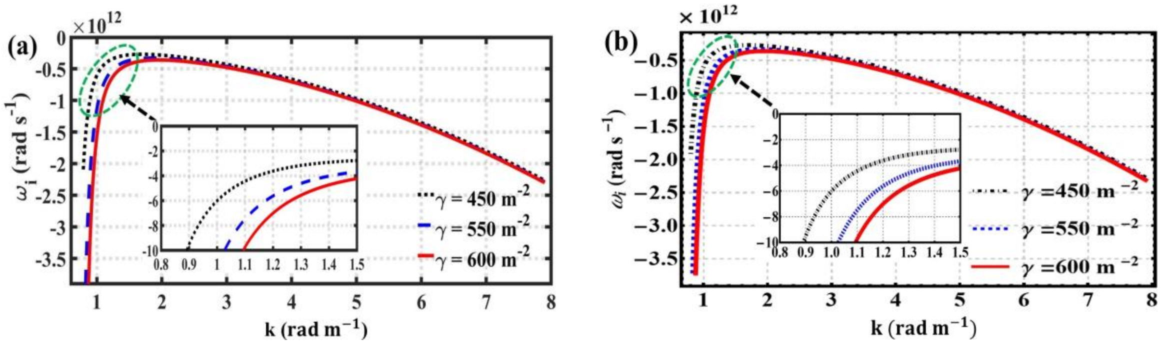

Figure 2.5: *Profile of the imaginary frequency part (ω_i) variation of the DR obtained for different γ-values with respect to k (a) analytically and (b) numerically. The different lines link to $\gamma = 450\ m^{-2}$ (black dotted line), $\gamma = 550\ m^{-2}$ (blue dashed line), $\gamma = 600\ m^{-2}$ (red solid line), respectively.*

Fig. 2.5 shows the ω_i-variation against k for different values of γ. The analytical (Fig. 2.5(a)) and numerical (Fig. 2.5(b)) plots are in good agreement for all values of k. Whereas, for larger values of k the plots are congruent with slight variation in magnitudes. The experimentally reported value of γ for hydrogen plasma is nearly $510\ \mathrm{m^{-2}}$ [17]. The ω_i-magnitude, while lower than ω_{spe} for $\gamma \approx 510$ m^{-2}, shows that the SPR remains trapped inside the IFB. This occurs due to its internal reflection from the inside of the sheath forming a standing acoustic wave like structure.

It may be highlighted that greater γ-value makes the density variation $[n_o = n_c \exp{(\gamma r^2)}]$ more pronounced within the IFB. This means that higher γ-values indicate a higher accumulation of charges in the IFB center, whereas the outer peripheries contain less charges. As a result, the SPI is more attenuated around the IFB center than anywhere else. Therefore, it may be inferred from the plots (Fig. 2.5) that γ is an SPI stabilizing parameter.

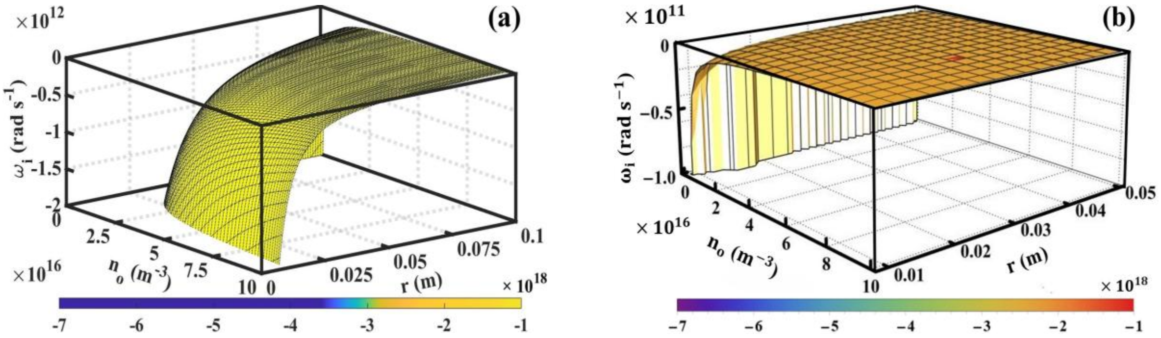

Figure 2.6: *Colormap profile depicting the (a) analytical and (b) numerical ω_i-variation with r and n_o [$= n_c exp\,(-\gamma r^2)$].*

Fig. 2.6 shows the collective variation of ω_i with respect to r and n_o. There may be minor discrepancies in the ordinate scaling (10^{12} in Fig. 2.6(a) (analytical) and 10^{11} in Fig. 2.6(b) (numerical)). It results in axis-parametric deviations originating from the two lowest-order terms expediently ignored in simplifying Eq. (2.16). It is noticed that ω_i increases with the increase in n_o, but the negative growth indicates the damping of the SPR. The large negative ω_i-magnitude at largest r and smallest n_o-values replicates that of 2-D profiles (Fig. 2.2) and proves that the SPR oscillation is internally reflected by the IFB sheath boundary. The larger ω_{spe}-value does not allow the instability to leak through the IFB boundary. Physics for the colormap (Fig. 2.6) is same as that explained in Fig. 2.2 which deals with both the density and radial distance variations.

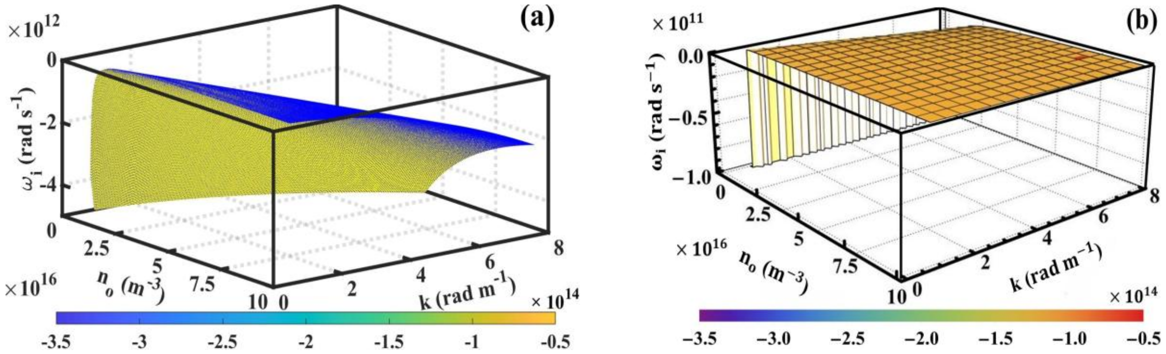

Figure 2.7: *Colormap depicting the (a) analytical and (b) numerical ω_i-variation conjointly with k and n_o [$= n_c exp\,(-\gamma r^2)$].*

For the SPR, both r and k are related by the expression $rk = (4\pi)^{-1}$. Hence, the modified SPR mode can be expressed in terms of k as $\omega_i = -316.51 i k^2 (1/m_e n_c) \exp\,(\gamma/16\pi^2 k^2)$. When k increases, the n_o also increases, and the ω_i-magnitude decreases. This behavior is opposite compared to the variation in ω_i with respect to r as shown in Fig. 2.7, since $r \propto k^{-1}$. Concisely, ω_i and k are directly proportional to each other up to a certain extent, beyond which they become inversely proportional. The same behavior is also noticed for ω_i varying with respect to n_o. The discrepancies in the graphical ordinate-scaling in Fig. 2.7(a) as 10^{12} (analytical) and in Fig. 2.7(b) as 10^{11} (numerical) with different multipliers, their quantitative graphical deviations, are the same as discussed before for Figs. 2.6(a-b). No such discrepancies are observed in the 2-D plots due to only one independent variable against two variables in the 4-D colormaps.

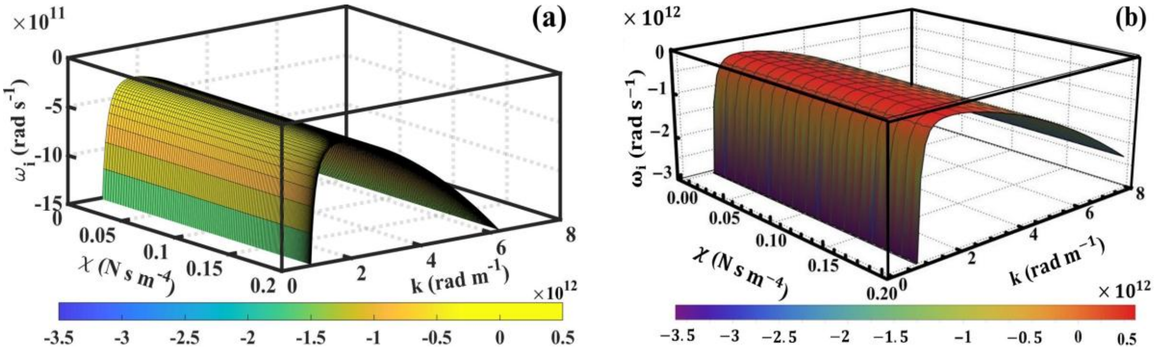

Figure 2.8: *Colormap profile depicting the (a) analytical and (b) numerical resonance ω_i-variation conjointly with $k = (4\pi r)^{-1}$ and χ $(= \xi k^2 + 2\beta/r^2)$.*

As in Fig. 2.4, SPR damping is noticed with the increase in k. It should be recalled that there is a variation of fluid viscosity with k. Therefore, any coordinate on the colormap is a triangulated outcome of all the three parameters, ω_i, $(\xi k^2 + 2\beta/r^2)$, and k. Here, k is the only independent parameter and the rest are dependent singly on k. The SPI mode remains trapped inside the IFB and forms a standing wave. It resembles the previously reported experimental data [5, 6], thereby corroborating the proposed bifluidic plasma fireball model approach.

After a series of comparisons between the analytical and numerical graphical results for ω_i-parameter, the numerically obtained nonzero ω_r-parameter is discussed hereafter. It may be reminded that the ω_r is found to be zero in magnitude in the analytical solution due to its small order of magnitude. Hence, the discussed ω_r-parameter afterwards is purely a yield of the numerical solution of the DR (Eq. (2.16)).

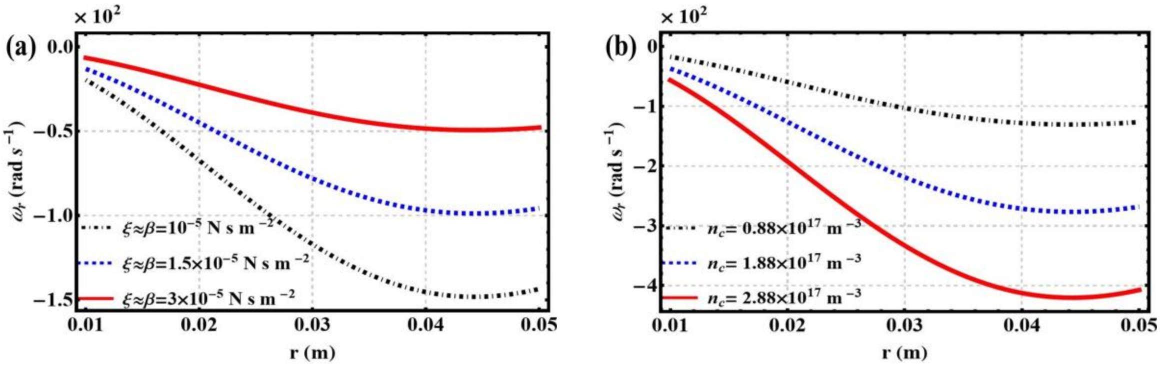

Figure 2.9: *Variation of ω_r for various (a) viscosity ($\chi \propto \xi$, β) and (b) central density (n_c) values with r at the resonance condition [$k = (4\pi r)^{-1}$].*

The distinct lines in Fig. 2.9 link to different ξ ($\approx \beta$) and $\mathrm{n_c}$ values indicated as (a) ξ ($\approx \beta$) $= 10^{-5}$ $\mathrm{N\,s\,m^{-2}}$ (black dotted line), 1.5×10^{-5} $\mathrm{N\,s\,m^{-2}}$ (blue dashed line), 3×10^{-5} $\mathrm{N\,s\,m^{-2}}$ (red solid line), and (b) $\mathrm{n_c} = 0.88 \times 10^{17}$ $\mathrm{m^{-3}}$ (black dotted line), 1.88×10^{17} $\mathrm{m^{-3}}$ (blue dashed line), 2.88×10^{17} $\mathrm{m^{-3}}$ (red solid line).

The observed characteristics of subplots in Fig. 2.9 are exactly opposite to those observed in Figs. 2.1-2.2 for the ω_i-parameter. In contrast to Figs. 2.1-2.2, larger n_c- and smaller $\xi(\approx \beta)$-values are found to yield higher ω_r-values (Fig. 2.9). Physics for this variation may again be attributed to the rising number density, thus plasma frequency towards the center, which strongly damps the instability.

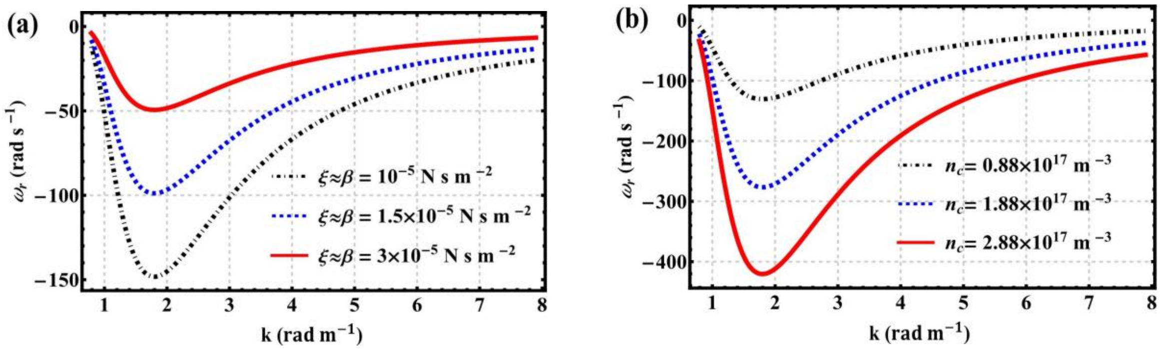

Figure 2.10: *Variation of ω_r for various (a) viscosity ($\chi \propto \xi$, β) and (b) central density (n_c) values with k at the resonance condition [$k = (4\pi r)^{-1}$].*

It is seen that Fig. 2.10 is comparable with Figs. 2.3-2.4. The corresponding maxima and minima of ω_i and ω_r for two different parameters [$\xi(\approx \beta)$, and n_c] form at common k-values.

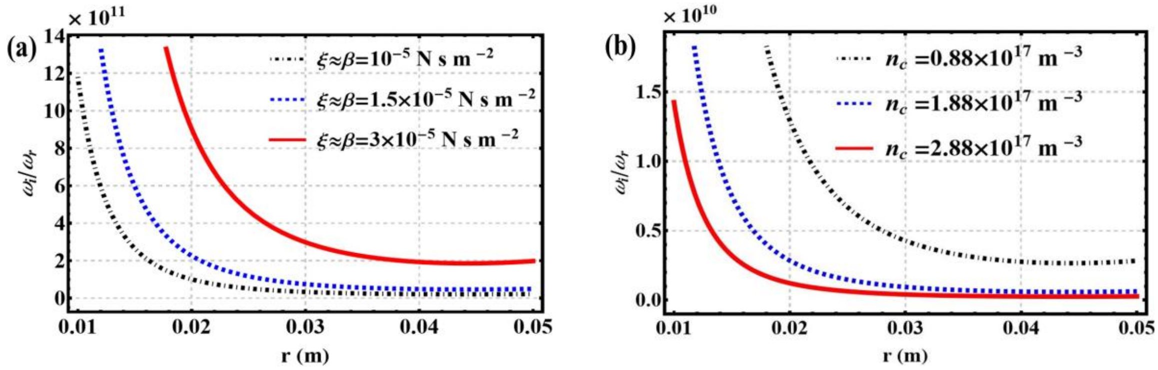

Figure 2.11: *Comparative profiles of ω_i and ω_r with respect to r for different (a) $\xi(\approx\beta)$ and (b) n_c-values.*

The spatial correlation of ω_i and ω_r for different parameters [$\xi(=\beta)$, and n_c] proves that the SPI ($\omega_i > 0$) and the evanescent wave formation ($\omega_r < 0$) occur simultaneously, and the latter is ubiquitous in the SPR.

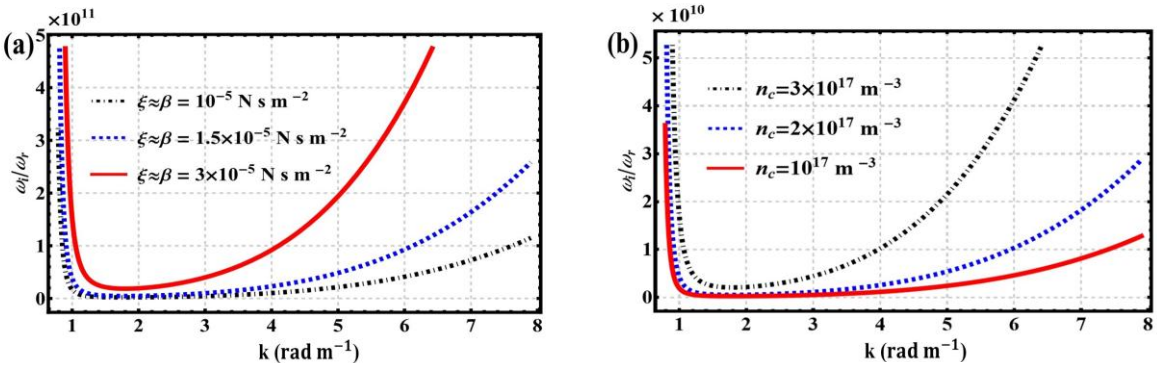

Figure 2.12: *Comparative profiles of ω_i and ω_r with respect to k for different (a) $\xi(\approx\beta)$ and (b) n_c-values.*

Fig. 2.12 compares the magnitudes of ω_i (instability or stability) and ω_r (propagation or evanescence) with respect to k for viscosity and density variations. The smaller ω_r-magnitude yields a larger ω_i/ω_r-ratio of order$\sim10^{10}$-10^{11}. Larger ω_i and smaller ω_r prove the standing wave-like and reflecting SPI-nature at the inner edge of IFB.

The respective rise and fall in the perturbation expressed through ω_i-variations are due to an increased plasma density close to the IFB center. The lower ω_r-value towards the IFB boundary (sheath region) indicates an evanescent SPI. The ω_r-parameter gradually approaching zero indicates a purely standing wave SPI at the IFB center.

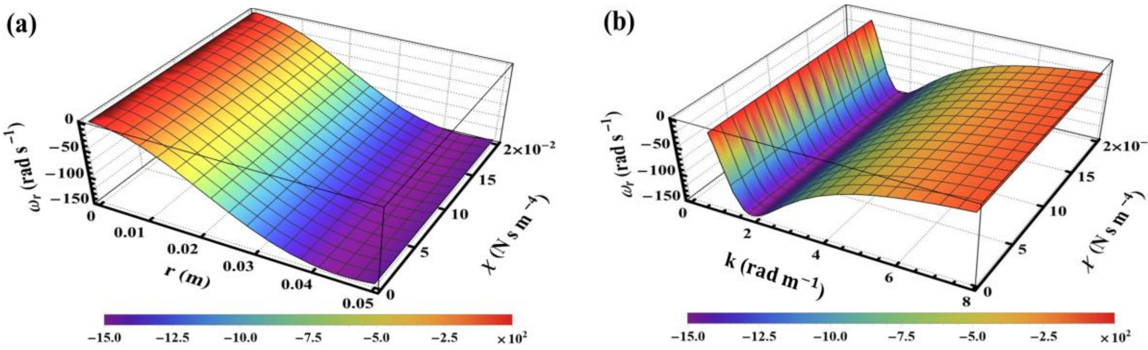

Figure 2.13: *Colormap showing the* ω_r*-profile with variation of* χ *evolving in (a)* r *and (b)* k.

It is noticeable that Fig. 2.6 and Fig. 2.14 illustratively show a similar variational pattern in ω_i and in ω_r, respectively. It is further seen that all the 2-D line profiles (Figs. 2.1-2.5, Figs. 2.9-2.12) and 4-D color profiles (Figs. 2.6-2.8, Figs. 2.13-2.14) from both the analytical and numerical outcomes corroborate each other. It justifies the reliability of our semi-analytical calculation scheme. It is further noteworthy that, the small jumps noticed in Fig. 2.14 (a) are purely mathematical outcomes stemming from the lowest-order coefficients, as already discussed in the case of Fig. 2.1 illustratively.

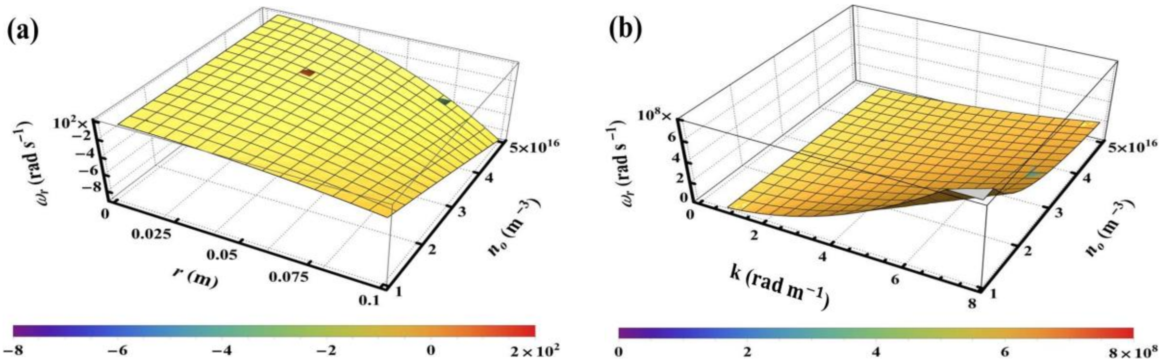

Figure 2.14: *4-D Colormap showing the collective variation of* ω_r *with respect to* n_o*, (a)* r*, and (b)* k.

The multi-parametric influences on the SPR stability features (Figs. 2.1-2.14) are now highlighted in Table 2.1 for the sake of instant reference of its readers. Besides, a tabular comparison of the analytical and numerical results is also presented in Table 2.2. It draws a relative contrast between these two sets of results by using two different software tools for graphical analyses. The similarities and the dissimilarities between the two sets of graphical results are highlighted in Table 2.2. Their fine matching expressed through their corresponding plots emboldens the accuracy of the SPR analysis.

Table 2.1: Multi-parametric SPR stability

S. No.	Physical parameter	Influence	Figure	Physical remark
1	Central density (n_c)	Weakly damping	Figs. 2.2, 2.4, 2.6, 2.7	Density fields act against the acoustic oscillations
2	Density steepness parameter (γ)	Damping	Fig. 2.5	Higher steepness increases the rate of damping at the IFB center and vice-versa
3	Effective viscosity ($\xi k^2 + 2\beta/r^2$)	Damping	Figs. 2.8, 2.13	High-viscosity plasmic shells prevent acoustic oscillations

Table 2.2: Analytical vs. numerical results

S. No.	Item	Contrast	Figure	Remarks
1	$\omega_i = \omega_i(r)$ for different ξ- values	Similar	Fig. 2.1	Two results corroborate
2	$\omega_i = \omega_i(r)$ for different n_c values	Similar	Fig. 2.2	Two results corroborate
3	$\omega_i = \omega_i(k)$ for different ξ-values	Similar	Fig. 2.3	Two results corroborate
4	$\omega_i = \omega_i(k)$ for different n_c values	Similar	Fig. 2.4	Two results corroborate
5	$\omega_i = \omega_i(k)$ for different γ values	Similar	Fig. 2.5	Two results corroborate

6	ω_r vs any other parameter	NA	Figs. 2.9-2.14	$\omega_r \approx 0$ for analytical solution and $\omega_r < 0$ for numerical solution

2.5 CONCLUSIONS

The SPR excitation physics in an IFB system is semi-analytically studied from the viewpoint of linear local perturbative treatment in a spherically symmetric geometry. The spherical symmetry makes the polar and azimuthal components redundant. The direction unbiased nature of the spherically symmetric fireballs nullifies the polar and azimuthal terms. Therefore, the polar and azimuthal parametric contributions are justifiably ignored for the sake of mathematical simplicity in the adopted calculation scheme. However, considering a non-spherical symmetry of the fireball structure or a nonzero applied magnetic field would make the polar and azimuthal components as significant as radial components for the plasma parameters, as well as the excited instabilities.

The basic structuring equations for portraying the electron and ion dynamics are linearized due to the assumed small-scale multi-parametric perturbations. This linearization enables us to ignore the nonlinear (higher-order) terms (multi-parametric cross-coupling effects) in the formalism of the plasma system. Moreover, the results of linear perturbation scheme manifest parameters directly influencing the stability or instability in the system. The electrostatic Poisson equation for the potential distribution yields the multi-parametric model closure as an intrinsic local model coupling property originating from the constitutive local charge density fields. The perturbed model system gets methodically decoupled into a quartic DR (Eq. (2.16)). The analysis theoretically demonstrates the SPR excitation in a reticular IFB in spherical geometry, unlike those found in the experimental arrangements, set up with central solid anodes. Such an SPR instability, studied here semi-analytically, has practically been observed and reported in solid anode experiments with typical plasma parameters: $n_e < 5 \times 10^{17}$ m^{-3}, $k_B T_e \leq$ 0.5 eV, and $P < 3 \times 10^{-4}$ Torr [6]. The typical variations in the magnitudes of the constant parameters [viz., n_c, $\xi (= \beta)$, and γ] considered in the graphical analyses (Figs. 2.1-2.4, 2.9-2.14) are in light of these experimental reporting on solid anode arrangement SPR studies. To the best of our knowledge, no SPR excitation has hitherto been reported experimentally in the literature for an IFB system developed within such hollow and reticular anodes as described above.

The obtained DR (Eq. (2.16)) is simplified by comparing the magnitudes of the multi-parametric coefficients through parametric substitution from an exemplary hydrogen plasma system [17]. The quartic equation is hence analytically reduced to a quadratic equation. It is noteworthy that among the four roots obtained, only one strong SPR mode is found to survive, with no propagation component ($\omega_r = 0$). It indicates that the SPR mode behaves as standing wave-like patterns in nature.

The quartic DR derived and solved analytically above, is now solved numerically, for analyzing the exact DR roots. This technique yields four different roots with fully distinct characteristics. However, only one out of the four roots produce feasible results, which are plotted in this work with respect to r and k. The lengthy numerical solutions are not presented here in detail. But the plots obtained from the solutions are used in the SPR analysis. A fair matching of the analytical and numerical solution patterns (for ω_i) proves the reliability of our calculation scheme. The numerically evaluated evanescent ($\omega_r < 0$, spatially constrained at the source) nature of the instability within the IFB sheath is also further validated with the help of obtained colourmaps (Fig. 2.14). Such evanescent modal features within the IFB originate due to the reflecting behavior of the sheath for the SPR frequencies, subcritical against the sheath plasma frequency, ω_{spe}.

The robustness of the numerical result can be manifested through feasible graphical plots prepared for different values of these plasma parameters. Three different numerical values for density $\{n_o = n_c \exp(-\gamma r^2)\}$ and viscosity (χ) are used for preparing the plots which prove the applicability of the derived solution within the given range.

The SPR develops in the sheath region and shows spatial variations of ω_i across the IFB. The externally biased IFB anode serves as the energy source for the SPI. As the density (n_o) and viscosity (χ) increase towards the IFB center from the sheath, the SPR disturbance starts damping. This quasi-stable SPR disturbance here shows a steep damping towards the IFB center after a finite traversal. Moreover, the SPR disturbance cannot leak through the sheath as the plasma frequency in the sheath region (ω_{spe}) is higher than ω_i-magnitude. So, it may be concluded that the IFB acts as a cavity resonator during the excitation of the SPR within it. It is because the IFB functions both as a cavity (shield) for the SPR excitations and as its sheath resonates with the internally trapped IFB plasma.

Along with SPR research, the fireball model is noticed to have many other applications in both pure and applied fields of active research and development. A few of these applications have been explored for decades, while the rest have been studied quite recently. Some of the focal investigative areas prevailing so far in the IFB context are briefly highlighted as follows:

(i) Antenna signals in spacecrafts: The spacecraft antennas get electrically charged in space and astroplasmic environments, thereby behaving further as electrodes with floating potentials. The possible excitations of the SPR in the antenna replicates with that in laboratory plasmas. Therefore, the laboratory SPR model studies could help in understanding antenna signal processing and subsequent applied diagnostics [5].

(ii) Coronal mass ejection: The Sun could usually be modelled as a huge plasma fireball in the thermonuclear fusion perspective. The magnetic turbulence associated with the solar sheath and subsequent coronal mass ejections (CMEs) could also be therewith studied. It is possible via fireball model formalisms in a scale invariant pathway as herein. These CMEs are interestingly active agents to yield major geomagnetic storms (as observed on the 20th of February 2023). It has been reported widely via the Wind/WAVES instrumentation and detection technology [18].

(iii) Junction diode analysis: The depletion region in a junction diode behaves as a plasma sheath. This region functions as a barrier in between the n- and p-type charges against diffusion, and the sheath functions as a similar potential barrier in between the electrode and ambient plasmas [19]. So, the proposed SPR analyses could be broadly useful for similar high-frequency diode-biasing experiments, observational analyses, and realistic applications extensively.

(iv) Sheath diagnosis: The SPR analysis reveals multiple plasma properties of great technological importance. It includes mainly the electron (ion) densities, electrostatic sheath potential, transient (displacement) currents, current-voltage characteristics, sheath electric field penetration and its shielding, ion ejection mechanism, potential relaxation oscillations, and so forth [20]. Such outcomes derived during an SPR study could be broadly useful to diagnose and characterize the involved plasma sheath structures in the said configurations comprehensively.

Apart from the above, the proposed model analysis could bring forward various future possible applicability and scope in more practical plasma environments. Such situations may involve highly nonlinear perturbations, presence of inhomogeneous magnetic fields, non-spherical geometries, nonlocal perturbations, and so forth. The study of SPRs in IFBs yields more physical insights into diverse plasma phenomena. It is shown here how SPR behaves inside an IFB illustratively. Besides, numerical and analytical outcomes are compared elaborately, resulting in reasonable corroboration. It is specifically shown herein that the SPR exhibits the collective excitation of evanescent standing wave patterns inside IFBs, subject to specific multi-parametric ranges. These waves fulfill the SPR condition. They are fully reflected by the plasma sheath, surrounding the IFB, thereby rendering it purely an internal IFB instability mode sourced in the free energy associated with the biased electrode (anode).

APPENDIX 2(A):
LINEAR AND QUASILINEAR SPR FEATURES

It may be expedient and convenient for the reader to highlight some of the relevant parameters of the linear SPI analysis using various formalisms alongside investigated characteristics alongside their corresponding quasilinear counterparts.

(a) Condition for linear SPR structure

The purely linear perturbation (small-scale) formalism applied in this work assumes that a perturbation in a relevant physical variable of the model system is so small that its rate of change varies directly as its instantaneous magnitude. For example, if a physical parameter, F undergoes a linear perturbation, F_1, then its spatiotemporal rate is proportional to its instantaneous state, mathematically given as

$$\frac{dF_1}{d(r,t)} \propto F_1(r,t). \qquad (2(A1))$$

Solving this proportionality equation with a constant on the RHS yields the exponential form of perturbation variation, i.e., $F_1 = F_{10}\exp\left(-i(\omega t - kr)\right)$ used in this SPR analysis within an IFB.

The above formalism allows us to examine whether the SPI pulses grow and reflect from the sheath or leak through it, by comparing the magnitude of the general solution of the DR (Eq. (2.31)) to the generic expression of ω_{spe} [21]. An experimental determination of the charge number density at the sheath (n_s) would help to figure out the magnitudes of other plasma parameters, and vice-versa. These equations can also be used to evaluate the limiting and threshold values of the relevant plasma parameters within which the IFB system can form evanescent SPI characteristics.

The DR solution and the generic expression for ω_{spe} [21] can be arranged analytically to yield the linear SPR condition given as

$$\left(\frac{1}{m_e n_c}\right)\left(\xi k^2 + \frac{2\beta}{r^2}\right)\exp(\gamma r^2) \leq 5.64 \times 10^4 \sqrt{n_s}. \qquad (2(A2))$$

If the LHS in Eq. (2(A2)) is greater than the RHS at $r = R$, where R is the radial distance of sheath from IFB center, the resonance condition will not be fulfilled and no SPR excitation will occur. In other situations, the SPR may still develop and reflect with LHS greater than the RHS, occurring at $r \neq R$, but it must be somewhere at $r < R$. It is noteworthy that, during the resonance, both r and k are interdependent through the linear SPR condition as $rk = (4\pi)^{-1}$.

In summary, the various possibilities derivable from Eq. (2(A2)) are highlighted as follows

$\omega_i(r = R) \leq 5.64 \times 10^4 \sqrt{n_s}$ (SPR occurs and gets reflected from the sheath), (2(A3))

$\omega_i(r = R) > 5.64 \times 10^4 \sqrt{n_s}$ (No SPR occurs), (2(A4))

$\omega_i(r < R) \leq 5.64 \times 10^4 \sqrt{n_s}$ (SPR occurs and gets reflected from the sheath), (2(A5))

$\omega_i(r < R) > 5.64 \times 10^4 \sqrt{n_s}$ (SPR may not occur at all). (2(A6))

The new ω_i-expression during the linear SPR behaviors in terms of r [with $k = (4\pi r)^{-1}$] as an independent variable mathematically reads as

$$\omega_i(r) = -\left(\frac{1}{m_e n_c}\right)\left(\frac{2\beta}{r^2}\right)\exp(\gamma r^2). \qquad (2(A7))$$

Similarly, new ω_i-expression during the linear SPR behaviors in terms of k [with $r = (4\pi k)^{-1}$] as an independent variable is mathematically given as

$$\omega_i(k) = -\left(\frac{1}{m_e n_c}\right)(32\pi^2\beta k^2)\exp\left(\frac{\gamma}{16\pi^2}\left(\frac{1}{k^2}\right)\right). \qquad (2(A8))$$

Hence, at the time of the SPI, the parameters r and k are interdependent. During the rest of the IFB operation, these two parameters may behave independently. Apart from other parametric values, r and k together yield the angular frequency (ω_i) magnitude.

(b) Condition for quasilinear SPR structure

The linear formalism discussed before is based upon the small-amplitude perturbation assumed in the analysis. Increasing the order of perturbation, however, may break the linearity condition as the rate of change of the perturbation and its instantaneous order (magnitude) are no longer proportional. This minimum magnitude of F_1 for which the proportionality relation (Eq. 2(A1)) loses its validity yields the quasilinearity. Unlike the linear treatment there is no pre-assigned form of perturbation and the same must be derived subsequently. A plasma parameter undergoing quasilinear perturbation is written as

$$F = F_o + \epsilon F_1 + \cdots \tag{2(A9)}$$

Where, F_o is the unperturbed parametric state, F_1 is quasilinearly perturbed state, and ϵ is a small parameter further denoting the amplitude of the quasilinear perturbation. Besides, ϵ also denotes a balanced strength between dispersion and convection [22]. It should be noted that further increase in the order of perturbation leads to nonlinearity in the system. A table comprising of various items showing the contrast between the linear and quasilinear formalism is presented in Table 1.2 to highlight the difference between the two.

REFERENCES

[1] Stenzel, R. L., Ionita, C. and Schrittwieser, R. Dynamics of fireballs. *Plasma Sources. Sci. Technol.*, 17(035006):1-11, 2008.

[2] Gruenwald, J. Reynvaan, J. and Knoll, P. Creation and characterization of inverted fireballs in H_2 Plasma. *Phys Scr.*, T61(014006):1-3, 2014.

[3] Stenzel, R. L., Ionita, C., and Schrittwieser, R. Neutral gas dynamics in fireballs. *J. Appl. Phys.*, 109(113305):1-8, 2011.

[4] Stenzel, R. L., Gruenwald, J., Ionita, C., Scrittwieser, R., Urrutia, J. M. Sheaths and double layers with instabilities. *J. Technol. Space Plasmas*, 2 (1): 70-91, 2021.

[5] Stenzel, R. L. Instability of Sheath-Plasma Resonance. *Phys. Rev. Lett.*, 60(8):704-707, 1988.

[6] Stenzel, R. L. High-frequency instability of the sheath-plasma resonance. *Phys. Fluids: Plasma Phys.*, 1(11):2273-2282, 1989.

[7] Chen, F. F. *Introduction of Plasma Physics and Controlled Fusion*. Plenum Press, New York, 1984.

[8] Bittencourt, J. A. *Fundamentals of Plasma Physics*. Springer Science + Business Media, 3rd Edition, New York, 2004.

[9] Dutta, S. and Karmakar, P. K. Fireball sheath instability. *J. Astron. Astrophys.*, 43(64):1-8, 2022.

[10] Karmakar, P. K. and Das, P. Nucleus-acoustic waves: Excitation, propagation, and stability. *Phys. Plasmas*, 25(8):082902(1-7), 2018.

[11] Degasperis, A., Holm, D. D. and Hone, A. N. W. A new integrable equation with peakon solutions. *Theor. Math. Phys.*, 133(2):1463-1474, 2002.

[12] Holm, D. D. and Hone, A. N. W. A class of equations with peakon and pulson solutions. *J. Nonlin. Math. Phys.* 12(1):380-394, 2005.

[13] Gruenwald, J. On the Dispersion relation of the transit time instability in inverted fireballs. *Physics of Plasmas*, 21(8):082109(1-5), 2014.

[14] Hasegawa, A. *Plasma instabilities and nonlinear effects*, vol. 8, Springer-Verlag, Berlin, Heidelberg, 1975.

[15] Gurnett, D. A. and Bhattacharjee, A. *Introduction to plasma physics*. Ed. 2, Cambridge University Press, Cambridge, United Kingdom, 2017.

[16] Wang, Y. and Du, J. The viscosity of charged particles in the weakly ionized plasma with power law distributions. *Phys. Plasmas*, 25(6):062309(1-8), 2018.

[17] Gruenwald, J. On the dispersion relation of the transit time instability in inverted fireballs. *Phys. Plasmas*, 21(082109), 2014.

[18] Ahamed, A. A., Subramanian, S. P., Rahman, A. M., Raja, A. K., Mahalakshmi, K., Thirumalaisamy, T. K. Study of solar activities with a Halo CME on 17 Feb 2023 event, *New Astronomy* 114(102312):1-7, 2025.

[19] DePaola, B. D. Diodes and transistors in practical analogue, digital, and embedded electronics for scientists. *IoP Publishing*, Bristol, UK, 2020.

[20] Stenzel, R. L., Gruenwald, J., Ionita, C. and Schrittwieser, R. Electron rich sheath dynamics. II. Sheath ionization and relaxation instabilities. *Phys. Plasmas*, 18(6): 062113(1-9), 2011.

[21] Huba, J. D. *NRL plasma formulary*. Plasma Phys. Div., Naval Research Laboratory, Washington, DC 20375, 2011.

[22] Dutta, S. and Karmakar, P. K. Sheath plasma instability in inverted fireballs. *Chaos Solit. Fract.*, 186(115259):1-12, 2024.